Chapter 10

Self-Assembly and Catalysis

10.1.1 Self-Assembly

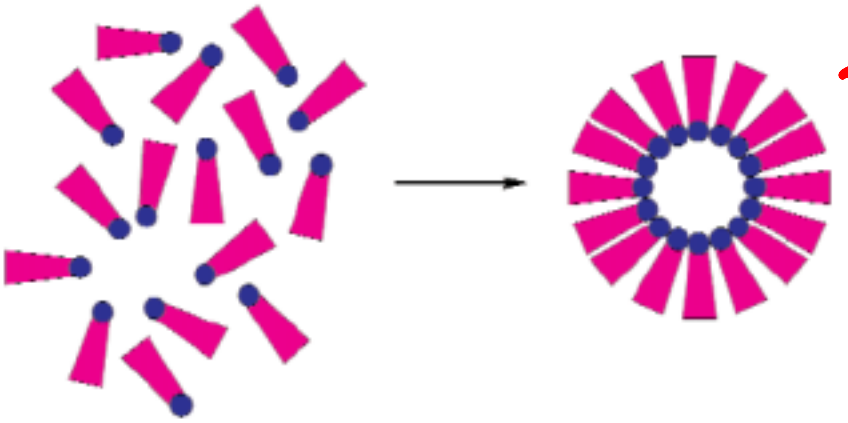

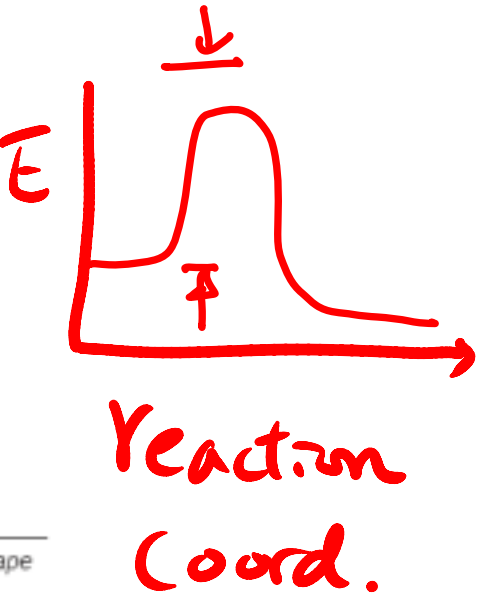

Figure 1. Illustration of basic self-assembly process. Individual wedges form a wheel shape as a result of chemical or physical interactions, with no outside intervention.

Traditional synthesis : kinetic control

Self-assembly : thermodynamic control

Covalent bond: ~100 Kcal/mole

Hydrogen bond: ~10 Kcal/mole

Van der Waals : ~1 Kcal/mole

Thermal energy: 3/2 kT at 300K
=> 0.45 Kcal/mole

10.1.1 Self-Assembly

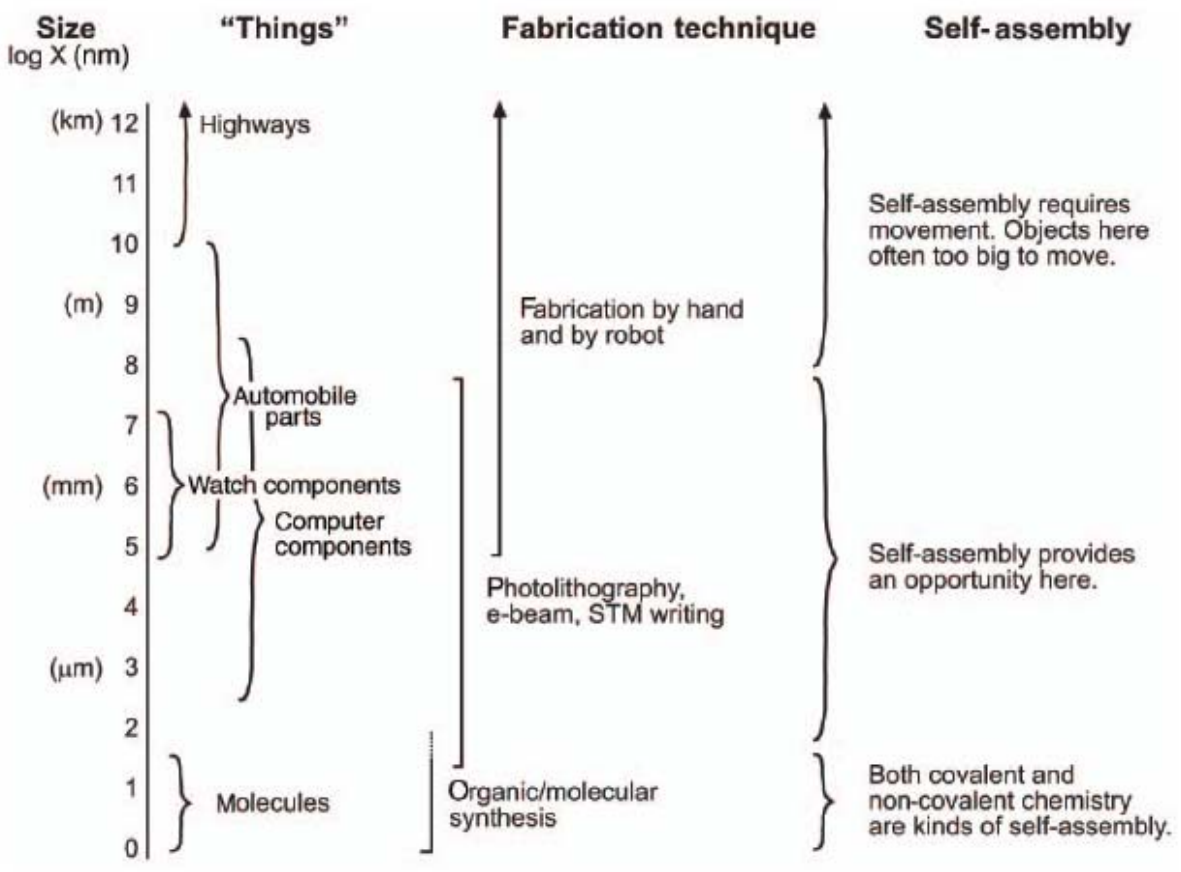

Figure 1. Chart illustrating the general scheme of "making things" at size scales ranging from nanometers to kilometers, and the possible niches for application of mesoscale self-assembly.

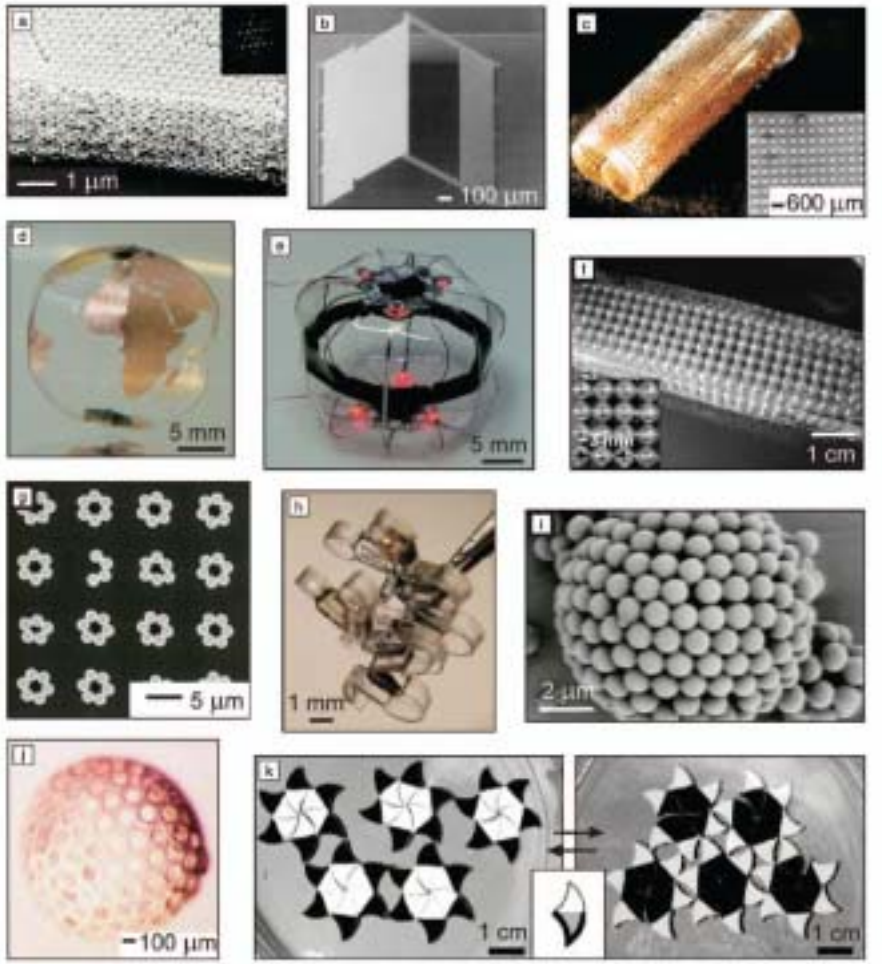

Figure 2. Examples of self-assembled mesoscale structures. (a) A hollow TiO_2 colloidal crystal. The inset shows Fourier transform of 40 μm × 40 μm region in the (111) plane of the crystal. (Reprinted in part with permission from Reference 25.) (b) An asymmetric, 3D silicon micromirror formed from a planar precursor by surface tension-powered self-folding. (Reprinted in part with permission from Reference 26.) (c) A large-area array of silicon segments self-assembled on a flexible, nonplanar support. The inset shows a detail of the structure. (Reprinted with permission from Reference 27.) (d) An elastomeric globe self-assembled from a flat, 2D projection of the Earth.[28] (Image: M. Bononeva.) (e) A simple 3D electrical circuit surrounding a spherical cavity. (Reprinted in part with permission from Reference 28.) (f) A self-assembled simple-cubic lattice of brass beads. The inset shows a detail of the structure. (Reprinted in part with permission from Reference 29.) (g) An array of ring-shaped aggregates of polystyrene beads. (Reprinted in part with permission from Reference 30.) (h) A 3D helical structure self-assembled from a crimped elastomeric tape. (Reprinted in part with permission from Reference 31.) (i) A dried hollow capsule (colloidosome) composed of polystyrene spheres. (Reprinted with permission from Reference 32.) (j) A porous sphere composed of hexagonal rings self-assembled on a drop of chlorobenzene in an aqueous silver-plating solution. (Reprinted in part with permission from Reference 33.) (k) Two different ratchet wheel structures with opposite chirality self-assembled from the same precursor plates. (Reprinted in part with permission from Reference 34.)

10.1.1 Self-Assembly

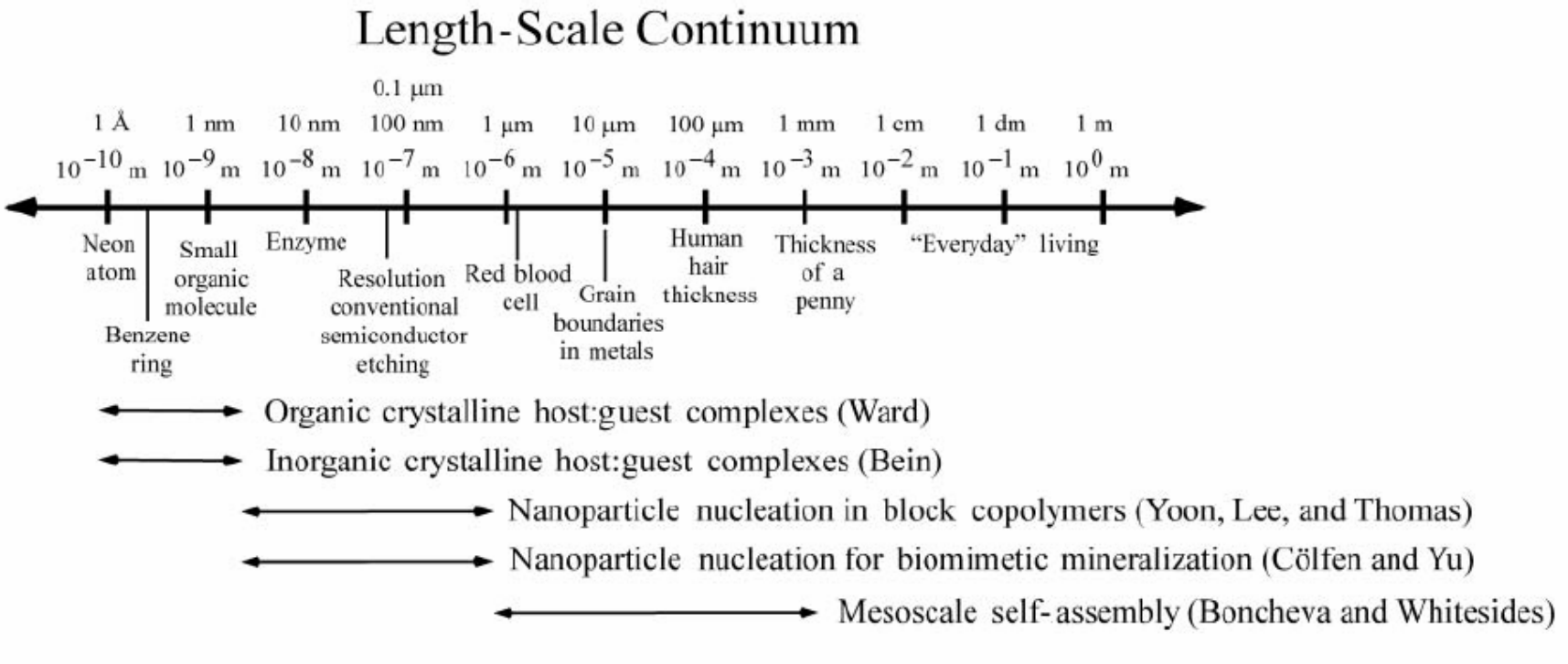

θ = 0 ~ 1 coverage

10.1.2 Semiconductor island

$$\frac{dn_1}{dt} = (R_{ads} + R_{det} + 2R_1) - (R_{evap} + R_{cap} + 2R_1')$$

vac layer

$$g = g_{sur-vac}(1-\varepsilon) + (g_{sur-lay} + g_{lay-vac})\varepsilon$$

surface

$$f = \frac{|a_f - a_s|}{a_s}$$

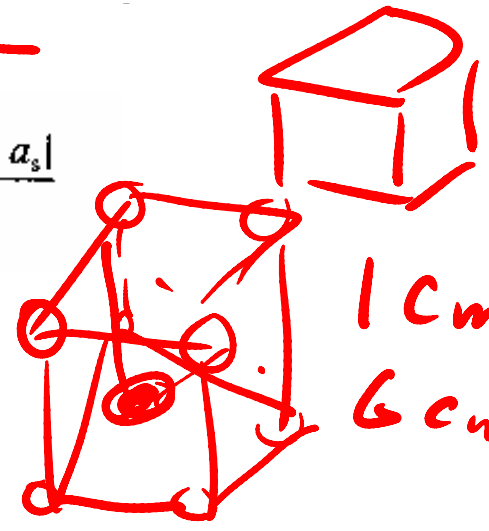

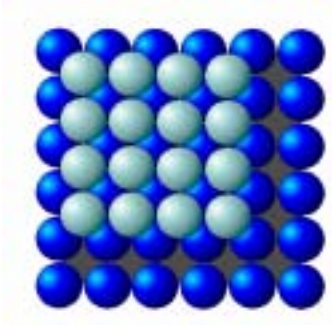

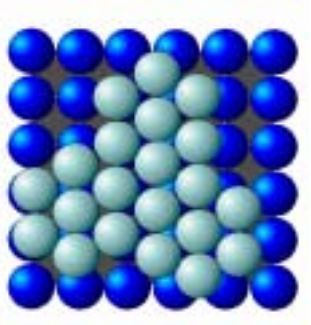

$\rho = 1\ g/cm^3$

$1\ cm^3$

$6\ cm^2$

$= \frac{6\times10^{23}}{18}\ /cm^3$

$10^{15}\ atom/cm^2$

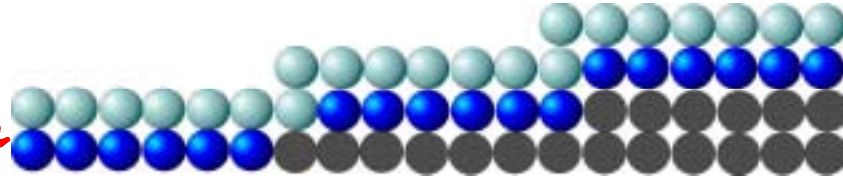

10.1.2 Semiconductor island

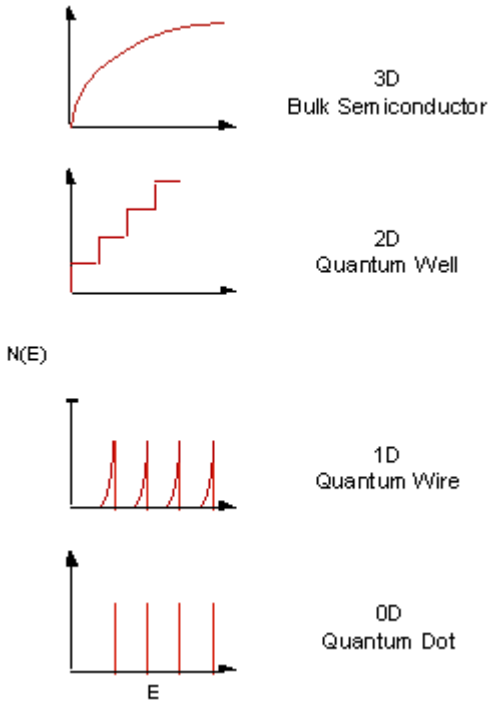

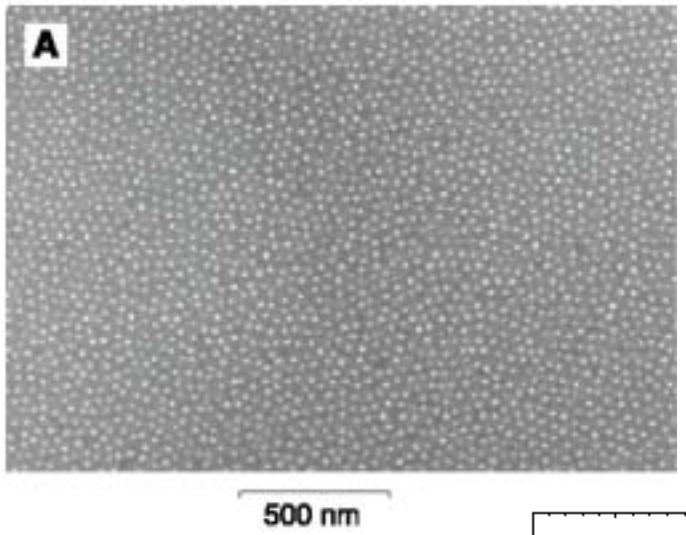

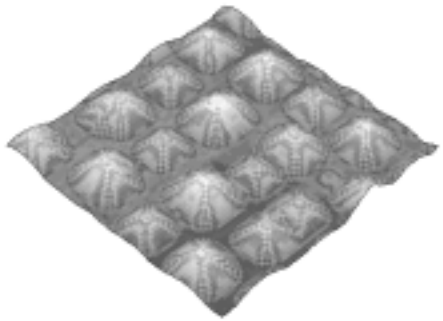

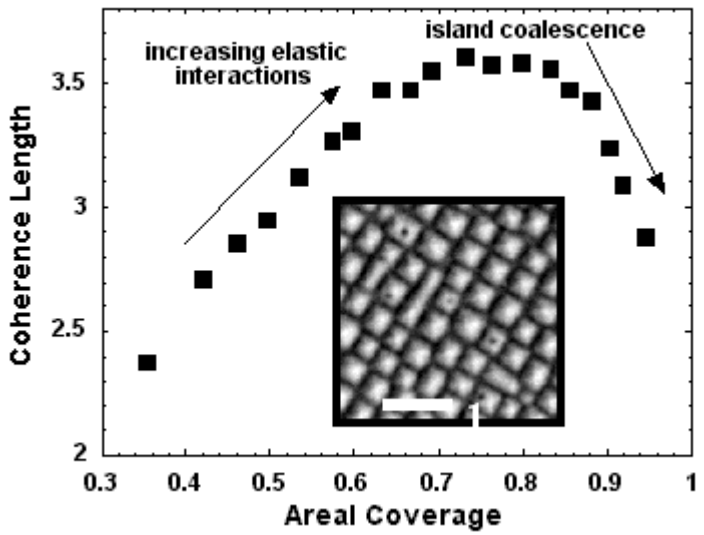

10.1.3 Self assemble monolayer

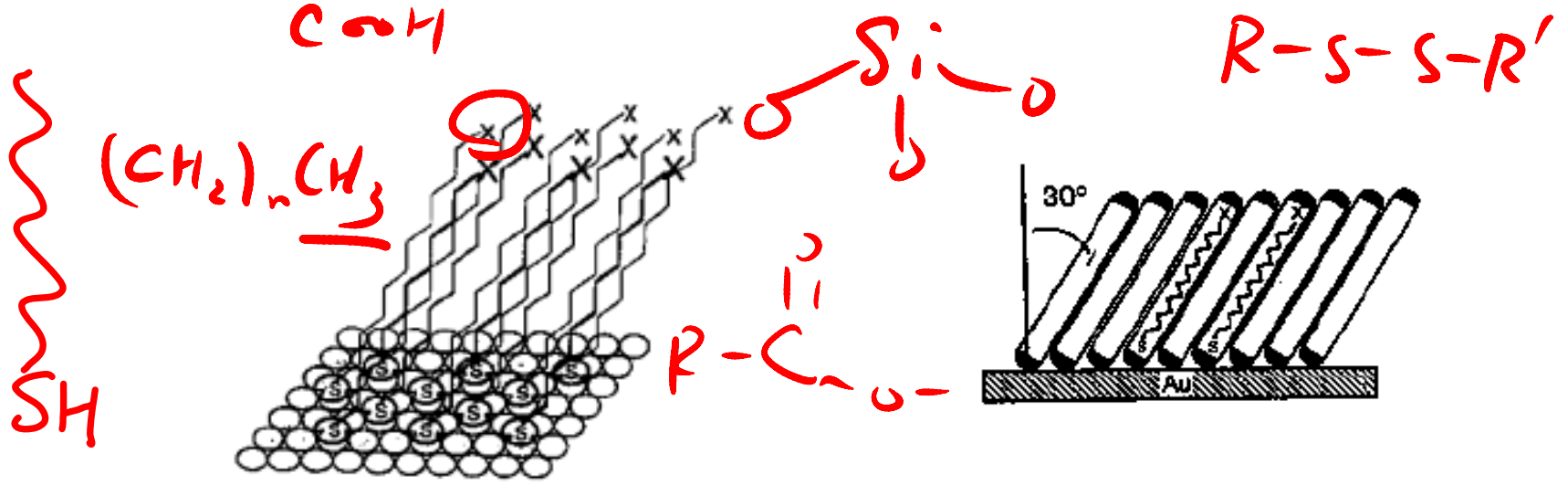

Figure 10.3. Illustration of the self-assembly of a monolayer of *n*-alkanethiolates on gold. The terminal sulphur resides in the hollow between three close-packed gold atoms, as shown in Fig. 10.2. The terminal groups labeled by X represent methyl. [From J. I. Wilber

M + S-S ⟶ S-M-S

$$CH_3(CH_2)_nSH + Au_m \Rightarrow CH_3(CH_2)_nS^-(Au_3^+)\cdot Au_{m-3} + \tfrac{1}{2}H_2$$

Au, Ag, Pt, Ni, Cu, Ge
Si, SiO_2, Glass

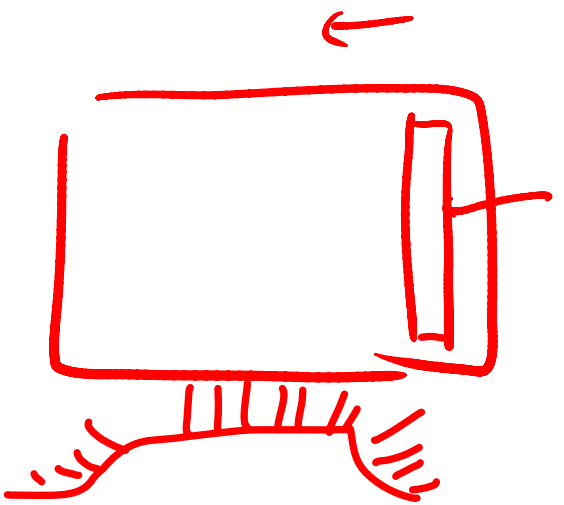

10.2 Catalysis

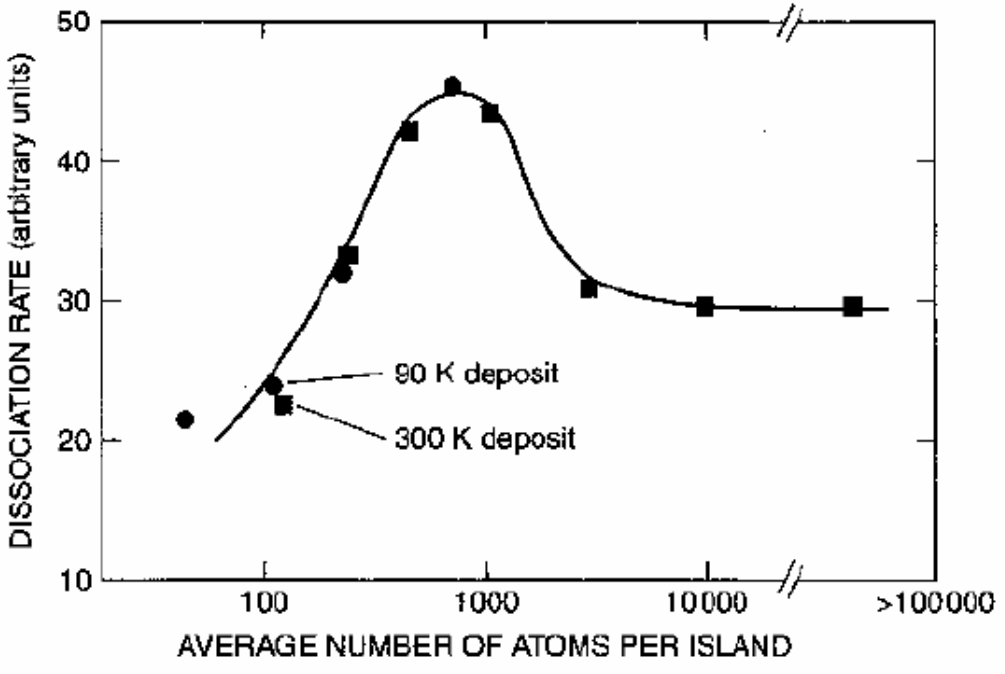

Figure 10.5. Effect of catalytic particle size on the dissociation rate of carbon monoxide. Rhodium aggregates of various sizes, characterized by the number of Rh atoms per aggregate, were deposited on alumina (Al_2O_3) films. The rhodium was given a saturation carbon monoxide (CO) coverage, then the material was heated from 90 to 500 K (circles), or from 300 to 500 K (squares), and the amount of atomic carbon formed on the rhodium provided a measure of the

10.2.2 Surface area

Unit : m^2/g

$$S = \frac{\text{area}}{\rho \cdot V} = \frac{4\pi r^2}{\rho \cdot \frac{4}{3}\pi r^3} = \frac{3}{\rho \cdot r}$$

○ → $V = \frac{4}{3}\pi r^3$

$A = 4\pi r^2$

$$= \frac{6}{(g/cm^3) \cdot nm} = \frac{6 \times 10^3}{\rho \cdot D\,(nm)} = \frac{6}{\rho \cdot D}$$

10.2.2 Surface area

Langmuir Isotherm

Langmuir suggests that adsorption takes place through this mechanism: $A_g + S \rightleftharpoons AS$, where A is a gas molecule and S is an adsorption site.

The direct and inverse rate constants are k and k_{-1}. If we define surface coverage, θ, as the fraction of the adsorption sites which are occupied, in the equilibrium we have

$$K = \frac{k}{k_{-1}} = \frac{\theta}{(1-\theta)P} \qquad \text{or} \qquad \theta = \frac{KP}{1+KP}$$

BET Isotherm

Often molecules do form multilayers, that is, some are adsorbed on already adsorbed molecules and the Langmuir isotherm is not valid. In 1938 Stephan Brunauer, Paul Emmett and Edward Teller developed an isotherm that takes into account that possibility. The proposed mechanism is now:

Ag + S ⇌ AS

Ag + AS ⇌ A2S

Ag + A2S ⇌ A3S and so on

Langmuir Isotherm

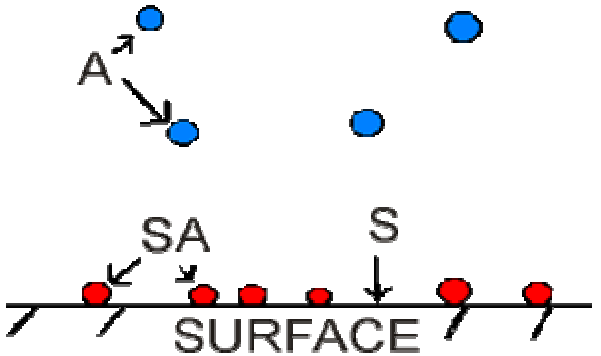

$$S + A \rightleftharpoons SA$$

$$K = \frac{[SA]}{[S]\,[A]}$$

$$b = \frac{\theta}{(1-\theta)P}$$

$$\frac{d\theta}{dt} = k_a\, p\, N(1-\theta)$$

$$\frac{d\theta}{dt} = -\,k_d\, N\,\theta$$

BET Isotherm

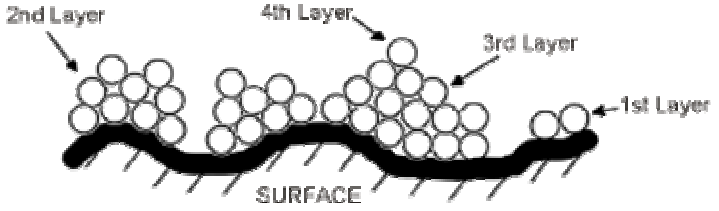

$$v = \frac{v_m c x}{(1-x)(1+(c-1)x)}$$

$$\frac{x}{v(1-x)} = \frac{1}{v_m c} + \frac{x(c-1)}{v_m c}$$

Langmuir and BET Isotherm

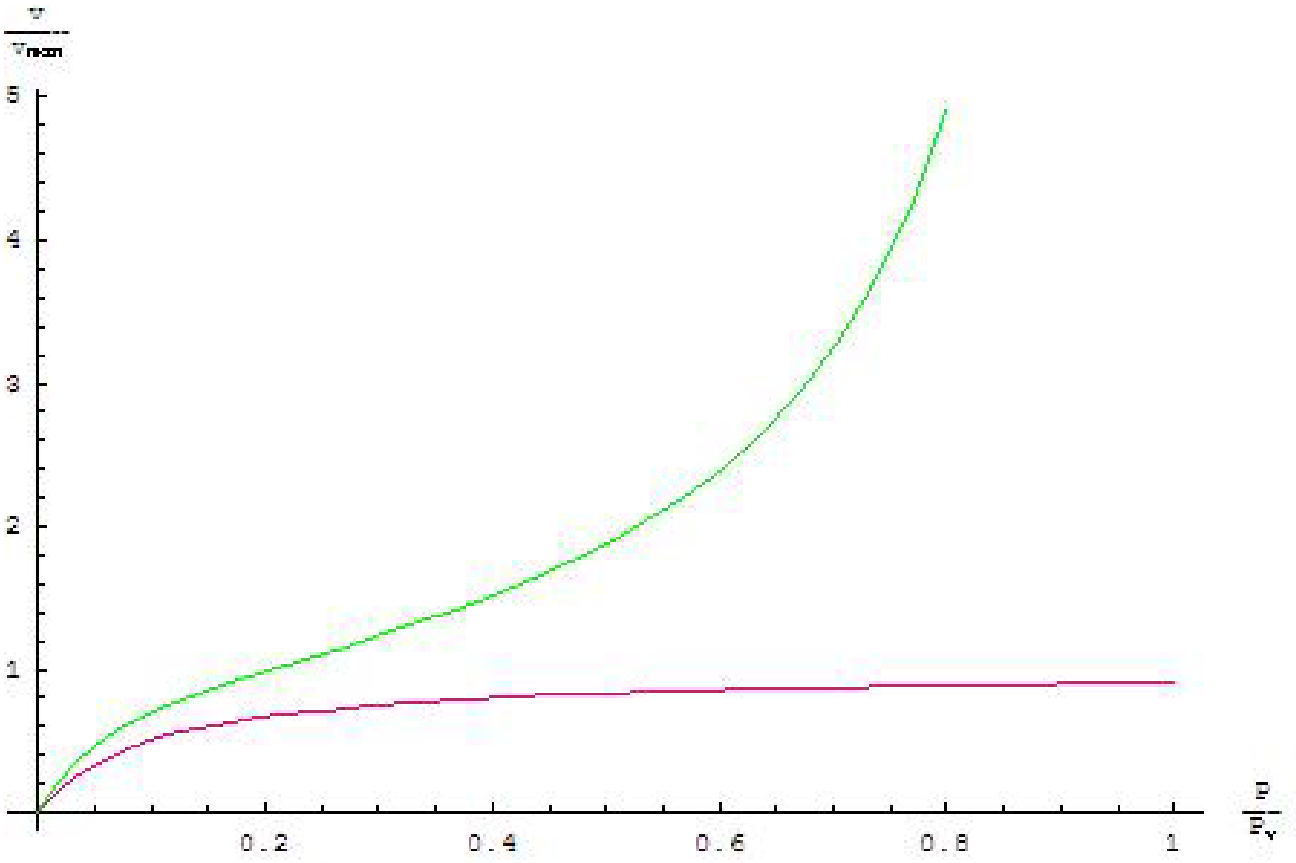

10.2.3 Porous materials

Scheme 1. Pore size distribution of various porous materials.

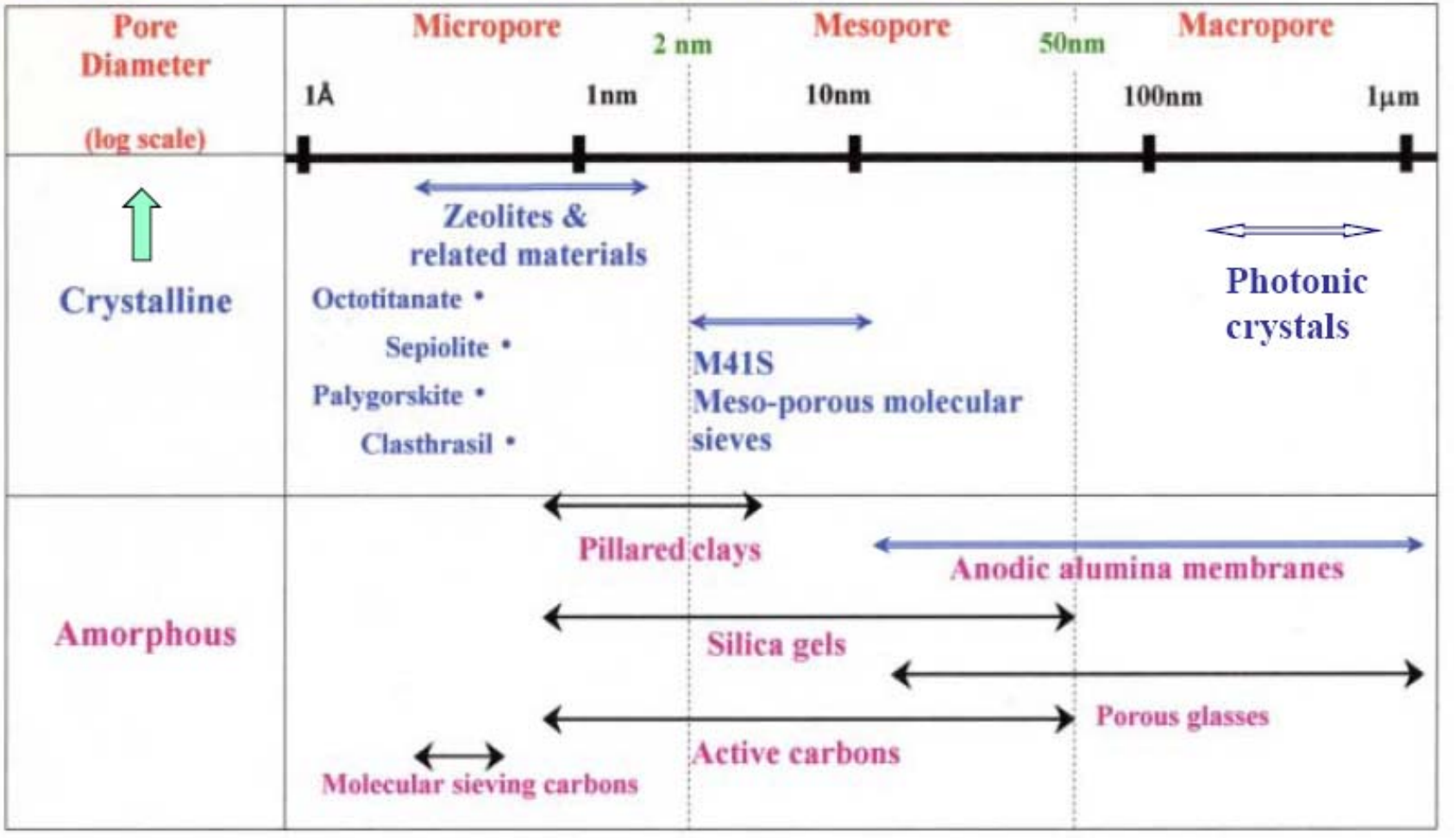

$(Ca^{2+}, Na_2)(Al_2Si_{10})O_{12} \cdot 8H_2O$

10.2.3 Porous materials

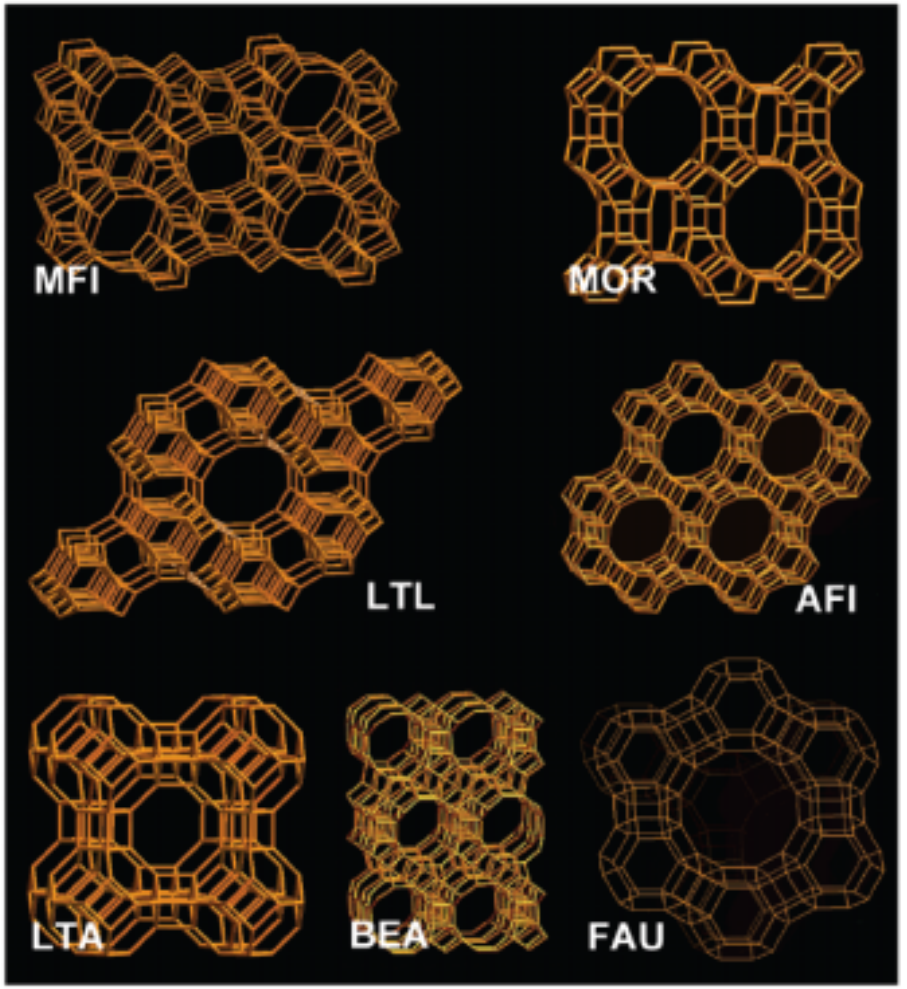

Figure 1. Structures of the seven zeolite types discussed in this article. The three-letter labels are structure codes. (From Reference 4.)

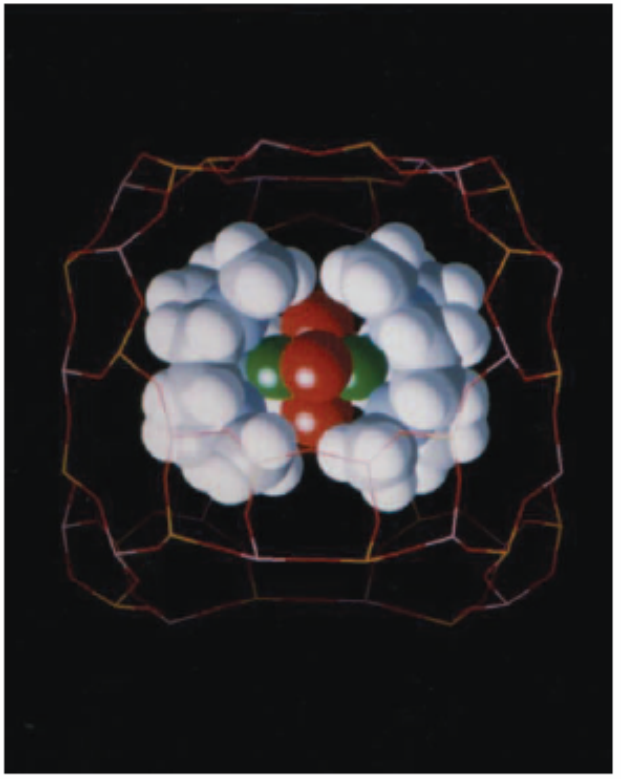

Figure 2. Formation of $[(L'Mn^{III}\text{-}(X)_3\text{-}Mn^{IV}(L')]^{n+}$ (n = 1–4) from manganese(1,4,7-trimethyl-1,4,7-triazacyclononane)$]^{2+}$ ($[(Mn(L')]^{2+}$) upon reaction with H_2O_2 in the cages of zeolite Y ($X = O^{2-}$, OH^-). L' is (1,4,7-trimethyl-1,4,7-triazacyclononane). (From Reference 12.)

Zeolites

Zeolites are microporous crystalline solids with well-defined structures. Generally they contain silicon, aluminium and oxygen in their framework and cations, water and/or other molecules wthin their pores. Many occur naturally as minerals, and are extensively mined in many parts of the world. Others are synthetic, and are made commercially for specific uses, or produced by research scientists trying to understand more about their chemistry.

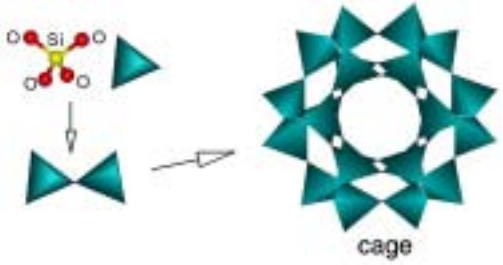

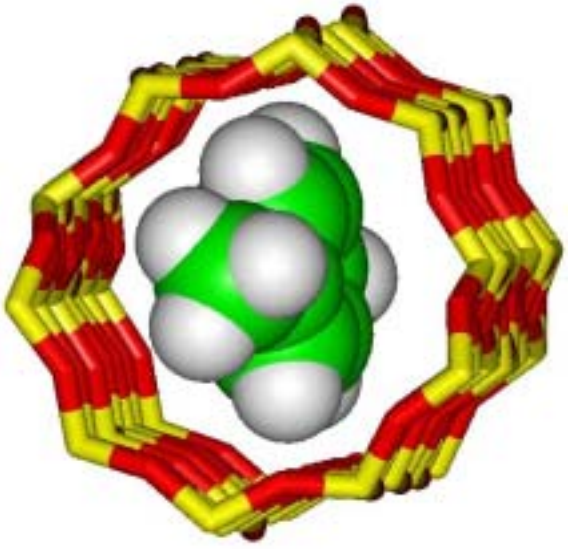

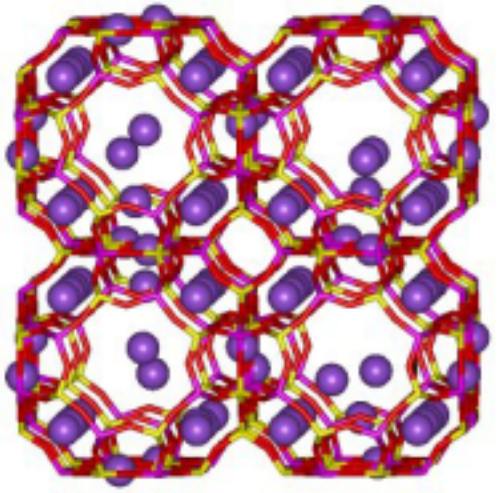

10.2.3 Porous materials

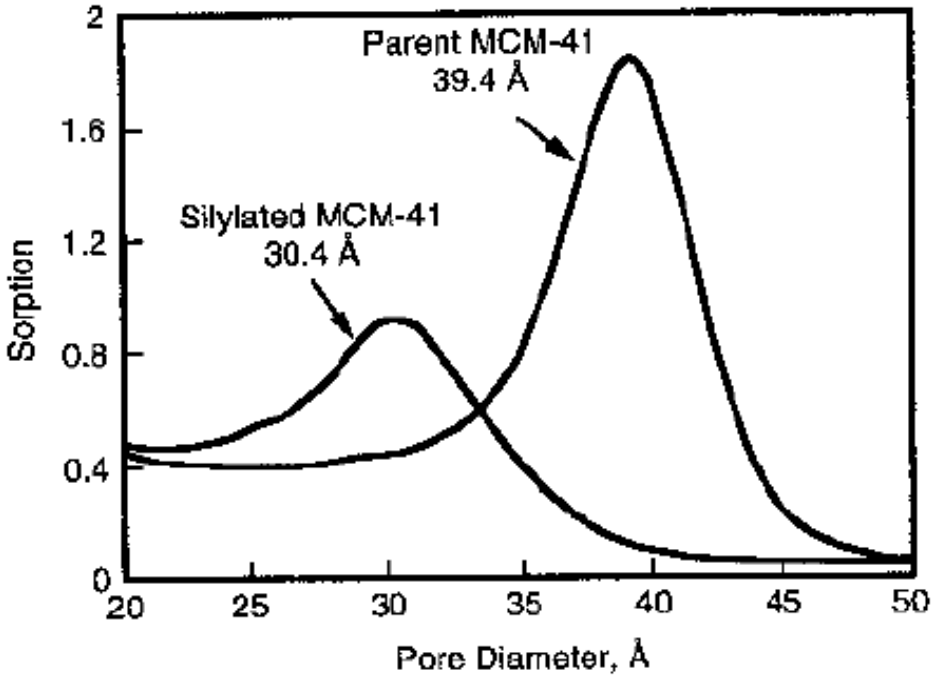

Figure 10.8 Distribution of pore diameters in two molecular sieves with mean pore diameters of 3.04 and 3.94 nm, determined by the physisorption of argon gas. [From J. S. Beck, J. C. Vartuli, W. J. Roth, M. E. Leonowicz, C. T. Kresge, K. D. Schmitt, C. T.-W. Chu, D. H. Olson, E. W. Sheppard, S. B. McCullen, J. B. Higgins, and J. L. Schenkler, *J. Am. Chem. Soc.* **114,**

Acidic Site

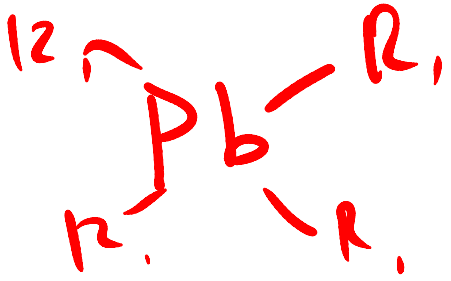

① proton donor

② electron acceptor

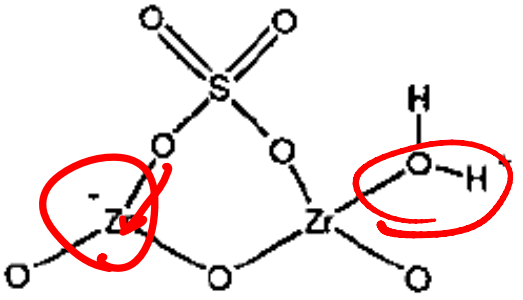

Figure 10.13. Configuration of sulphate group on the surface of a zirconia–sulfate catalyst, showing the Lewis acid site Zr^{-} at the left, and the Brønsted acid site H^{+} at the right. [From

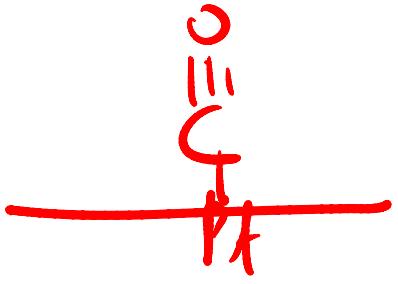

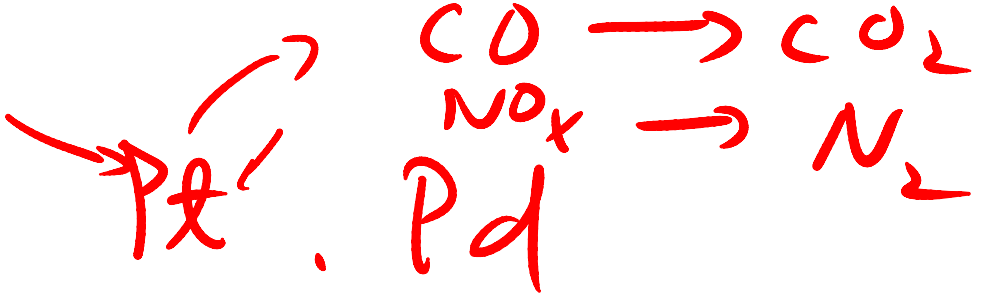

10.2.4 Clays

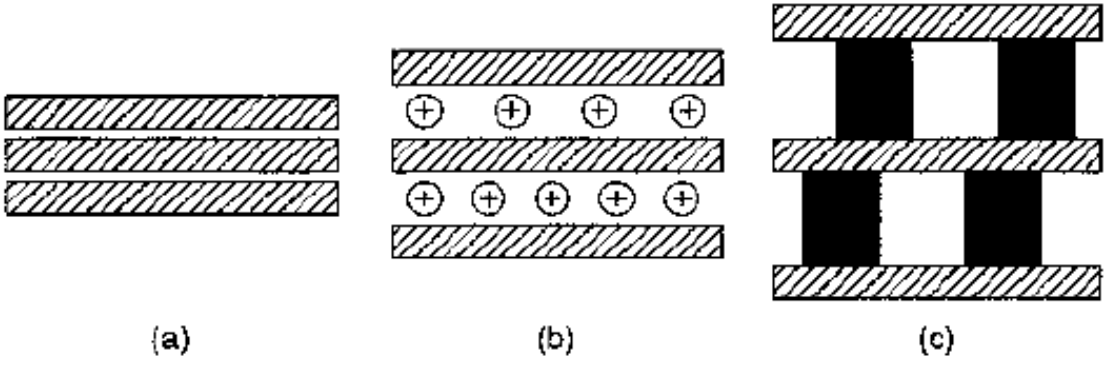

Figure 10.15. Saponite clay layers shown (a) before adsorption (b) after adsorption of cations

10.2.5 Colloids

1 ~ 1000 nm

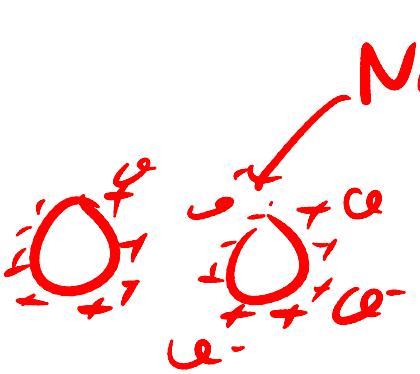

organosol : colloid in organic liquid

hydrosol in water

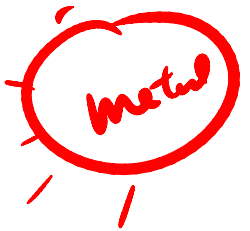

$NR_4X \rightarrow NR_4^+ + X^-$

10.2.5 Colloids

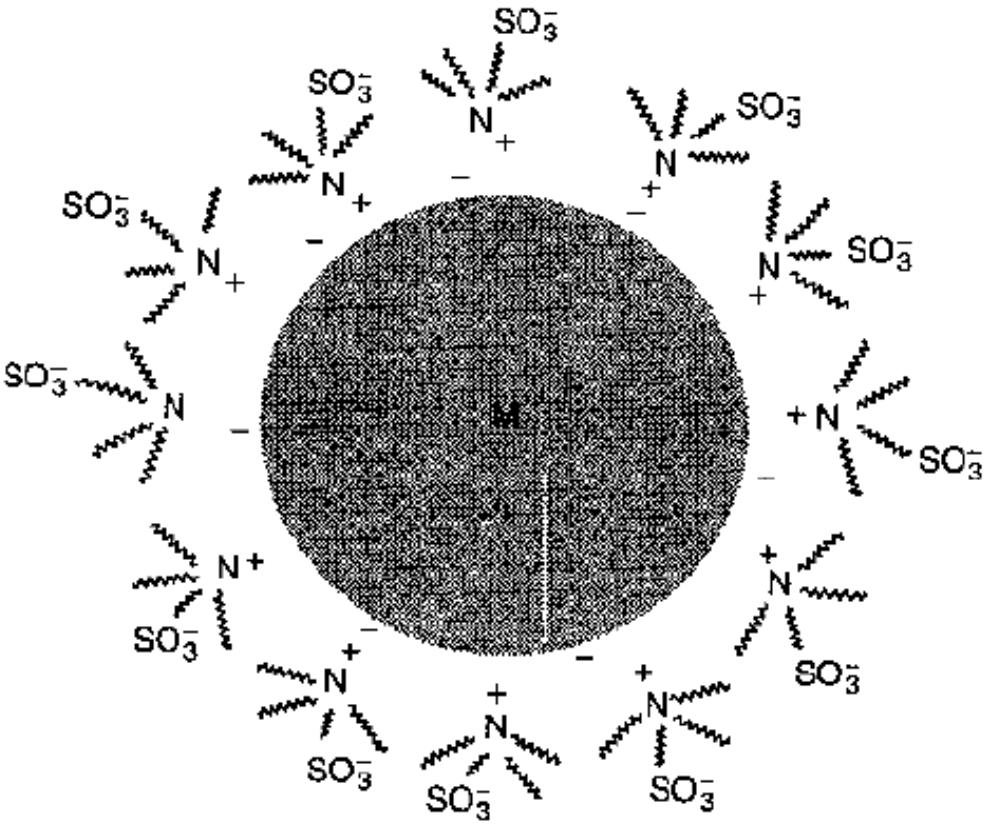

Figure 10.23. Metallic colloidal particle stabilized by sulfobetaine compounds related to NR_4X, but with an SO_3^- group at the end of one of the alkyl chains R. [From H. Bönnemann and W. Brijoux, in Moser (1996), Chapter 7, p. 174.]

Chapter 11

Organic Compounds and Polymers

11.2 Polymer

monomer

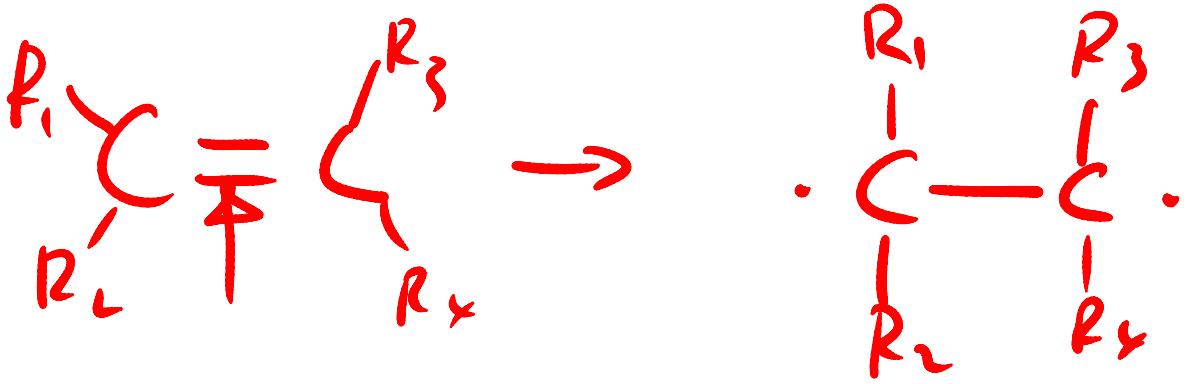

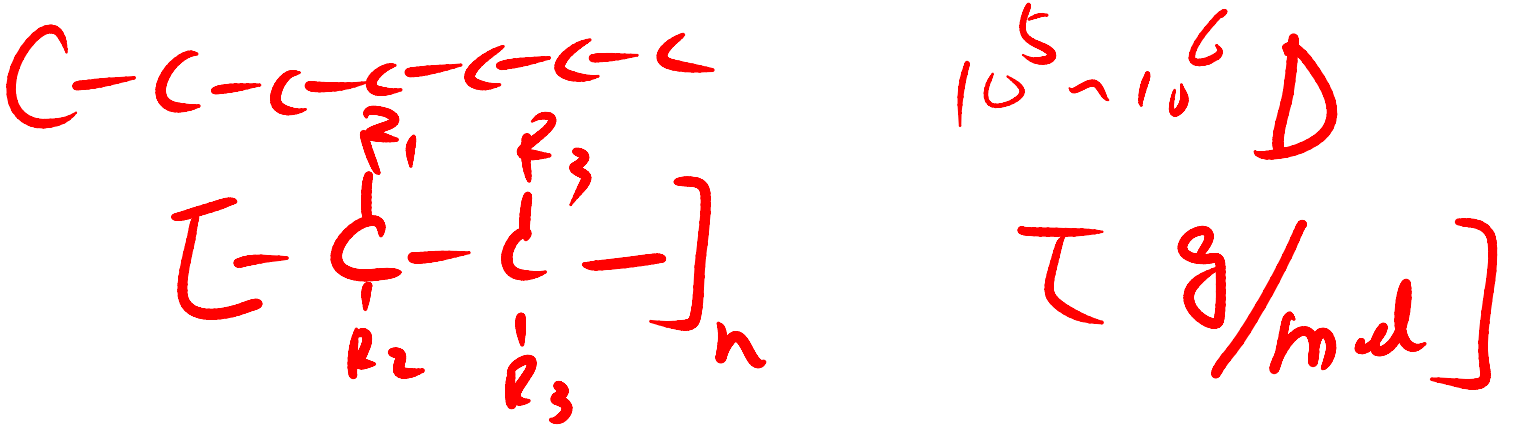

11.2.2 Size of polymers

$$V\,(cm^3) = \frac{M_w}{\rho} \times 1.66 \times 10^{-3}$$

g/mole → # 6×10^{23}

g/cm^3

nm^3

$$V = d^3 = 1.66 \times 10^{-3} \frac{M_w}{\rho}$$

$$\Rightarrow d = 0.118 \left(\frac{M_w}{\rho}\right)^{1/3}$$

d → nm

Homework : relationship for spherical polymer

11.4.1 Conducting Polymers

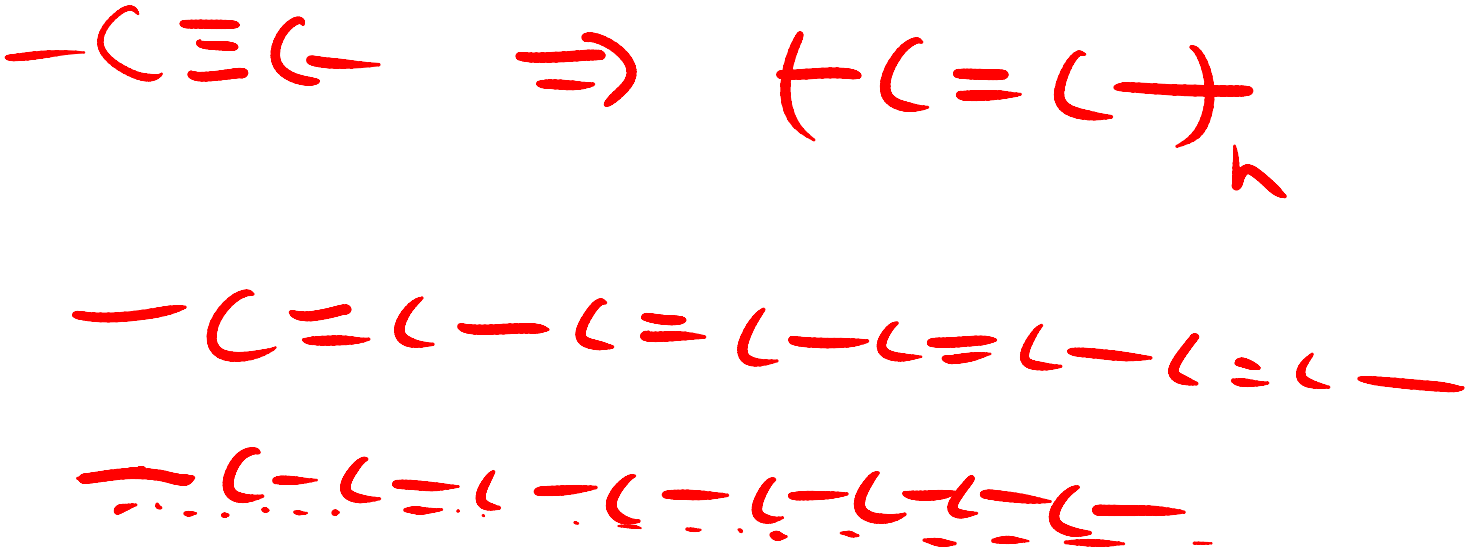

11.4.2 Block copolymers

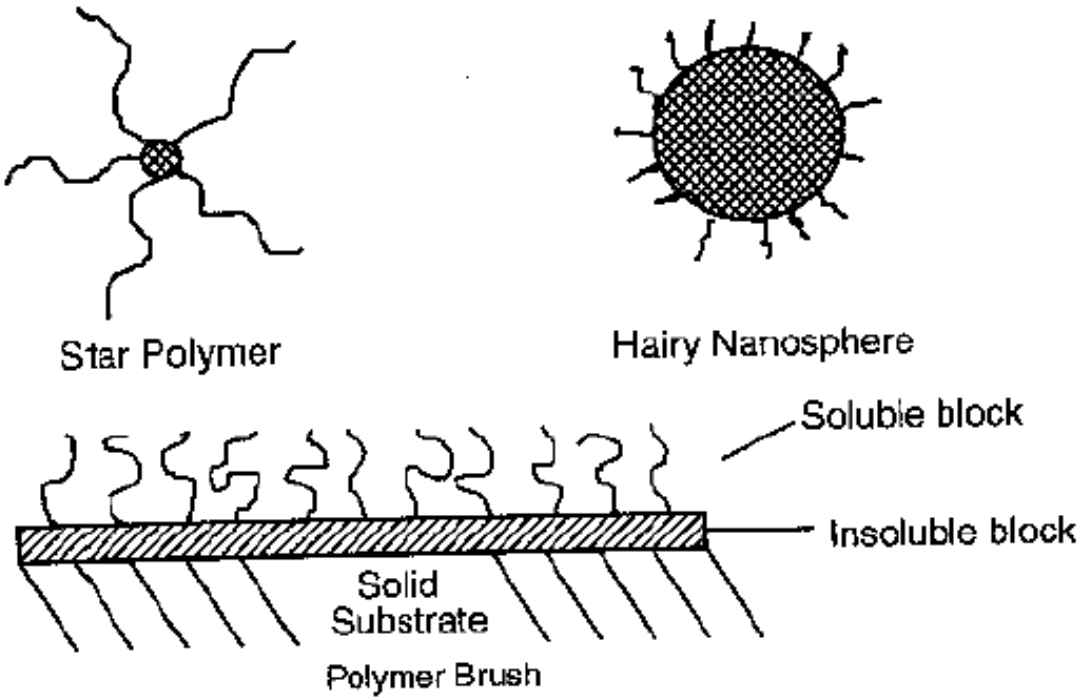

11.4.2 Block copolymers

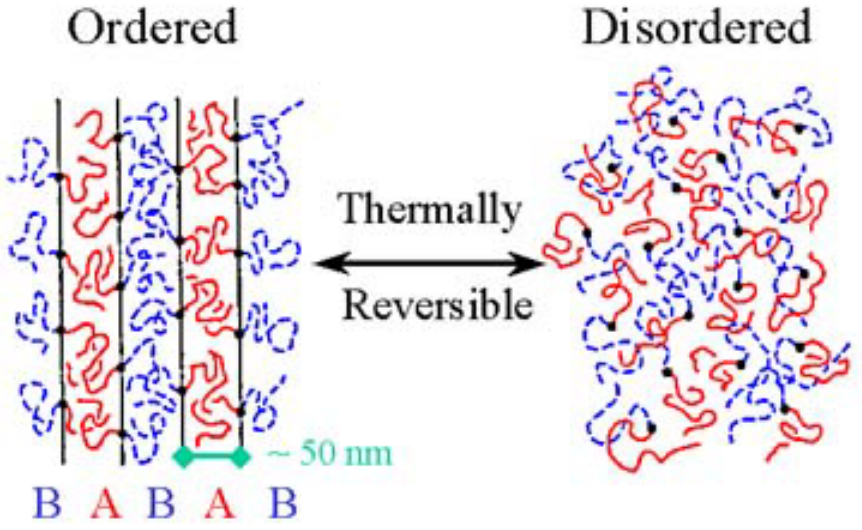

end – poly A – transition – poly B – end

11.4.2 Block copolymers

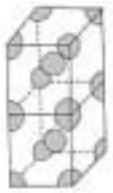

Spheres (BCC)

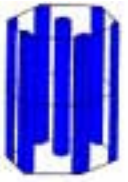

Cylinders (HEX)

Gyroid (GYR)

Lamellar (LAM)

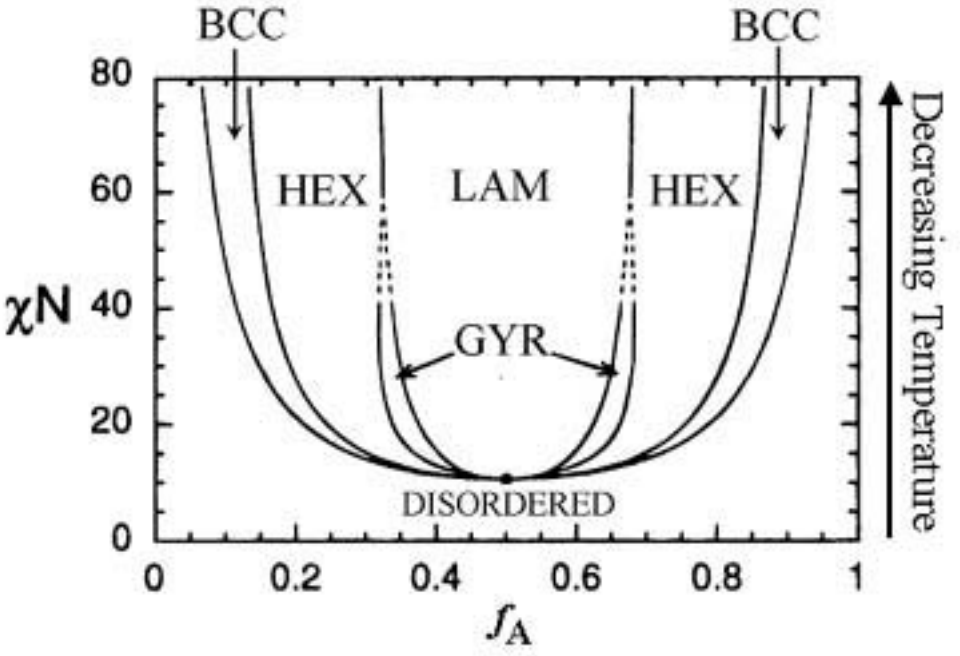

11.4.2 Block copolymers

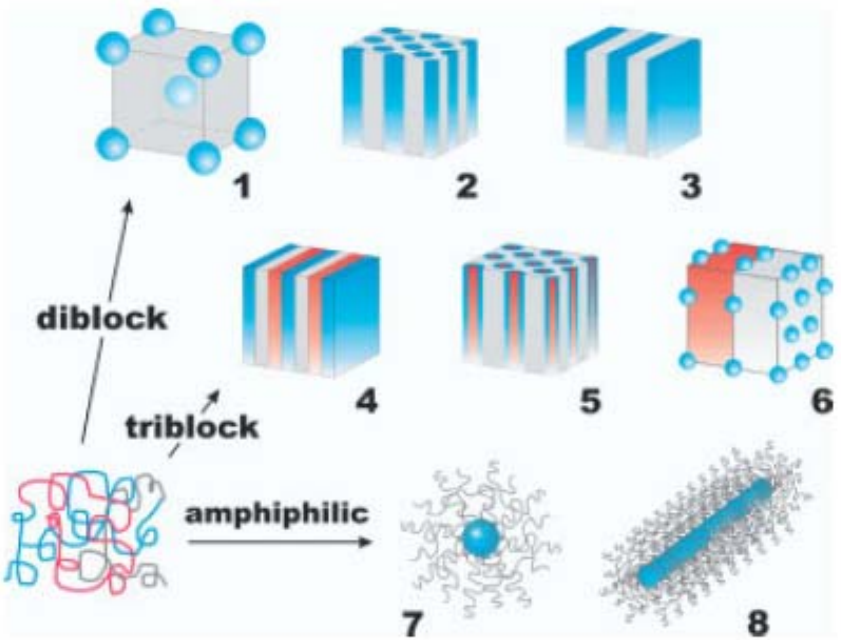

Fig. 1. Sketches of equilibrium morphologies from BC self-assembly, among the most frequently used for nanofabrication. For diblock copolymers in bulk: body-centered cubic-packed spheres (1), hexagonally ordered cylinders (2), lamellae (3). For triblock copolymers: lamellae (4), hexagonal coaxial cylinders (5), spheres between lamellae (6). For amphiphilic BCs in solution: spherical micelles (7), and cylindrical micelles (8). Periodicities, or micellar dimensions, are in the range 10–100 nm.

Block Copolymer as Photonic Materials

high-dielectric material about a template

1.6:1) (Figure 2c).

However, it turns out that the double gyroid network structure does not possess

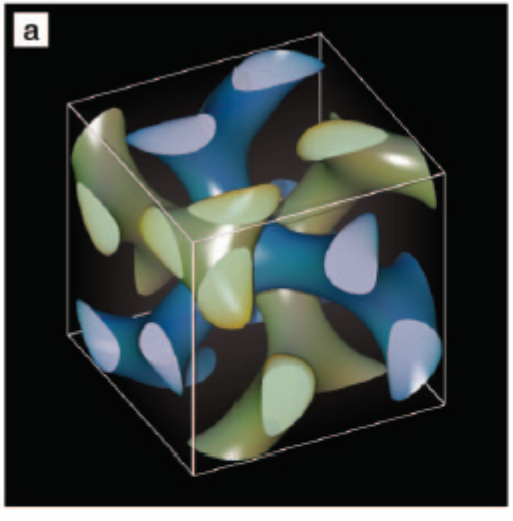

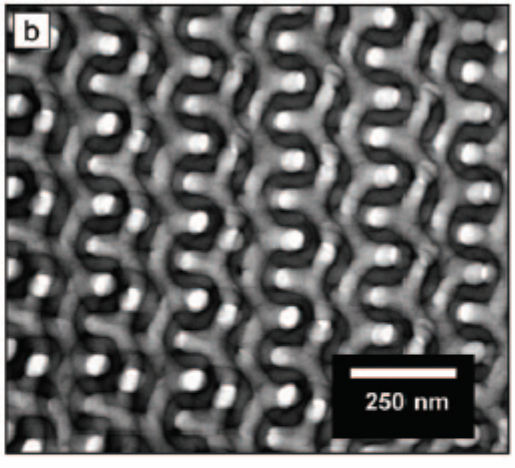

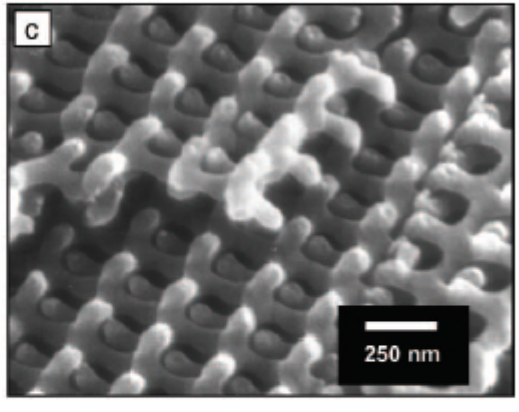

Figure 2. (a) Schematic illustration of the unit cell of the double gyroid morphology. The double gyroid structure comprises two interpenetrating three-dimensionally continuous networks of the minority component (shown in blue and yellow to help in visualization). (b) Transmission electron micrograph of an 80-nm-thick cryo-microtomed thin section of the 750 kg/mol PS–PI block copolymer. The image is of the [123] projection of the microstructure, yielding a lattice parameter of the cubic cell of 250 nm. The isoprene matrix has been stained with osmium tetroxide, leaving the styrene networks light in this bright-field micrograph. (Reprinted with permission from Reference 26.) (c) Scanning electron microscopy secondary electron image of the double gyroid styrene networks remaining after UV/ozone etching, showing that the networks remain intact and self-supporting after processing. The dimensions of the network structure are not perceptibly changed by the processing. (Reprinted with permission from Reference 26.)

Block Copolymer as Photonic Materials

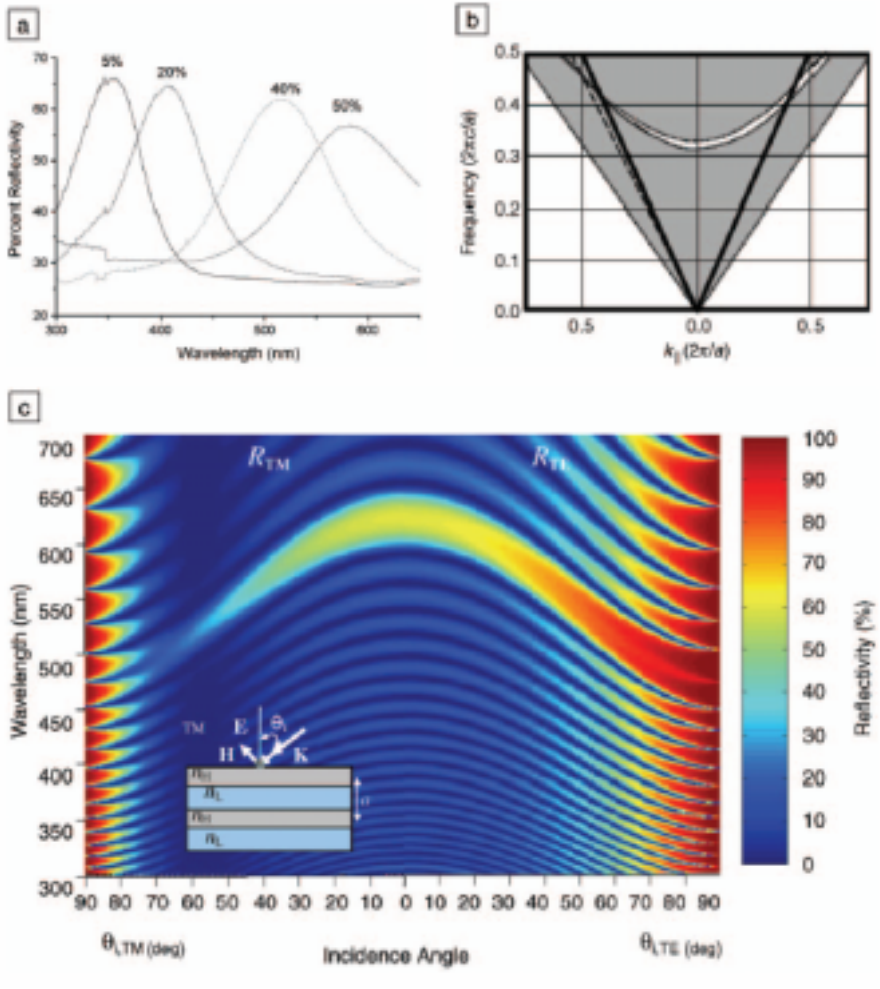

Figure 1. (a) Reflectivity of ternary block copolymer (PS–PI with 194 kg/mol of PS block and 197kg/mol of PI block)/homopolymer (13kg/mol of PS and 13kg/mol of PI) blends containing 5%, 20%, 40%, and 50% added homopolymer, respectively. The progression of the stop band to longer wavelengths and broader peaks with increasing homopolymer content is evident. (Reprinted with permission from Reference 17.) (b) A band diagram (dimensionless frequency versus dimensionless wave vector) using the refractive indices of polystyrene (PS) and polyisoprene (PI) and the layer thicknesses of a PS-b-PI/PS/PI blend (c is the speed of light in a vacuum, a is the lamellar domain periodicity). The transverse-electric (TE) polarization modes are on the right side, and the left side is for the transverse-magnetic (TM) polarized light. The shaded regions represent allowed propagating modes. The dotted curves are the band edges. The partial bandgap is the thin, crescent-shaped region between the second and third bands. The region between the solid black lines (the "light lines") defines the region of the diagram accessible to light incident from outside the material. The dashed curve on the left side of the graph is the Brewster line, the angle where TM polarized light passes through the structure without reflection. (Reprinted with permission from Reference 16.) (c) Reflectivity plot constructed by the transfer matrix method for a 20-period stack of alternating PS and PI layers, where R_{TM} and R_{TE} represent the reflectivity for TM and TE polarization, respectively. Each layer is assumed to be 100 nm thick. The color represents the strength of the reflectivity at a particular frequency and angle of incidence. The inset shows a schematic of TM polarized light incident on the multilayer stack with an angle θ_i (E – electric field vector, H – magnetic field vector, k – wave vector, n_H – refractive index of high-index layer, n_L – refractive index of low- index layer, a – domain periodicity).

11.5.2 Dentritic Molecules

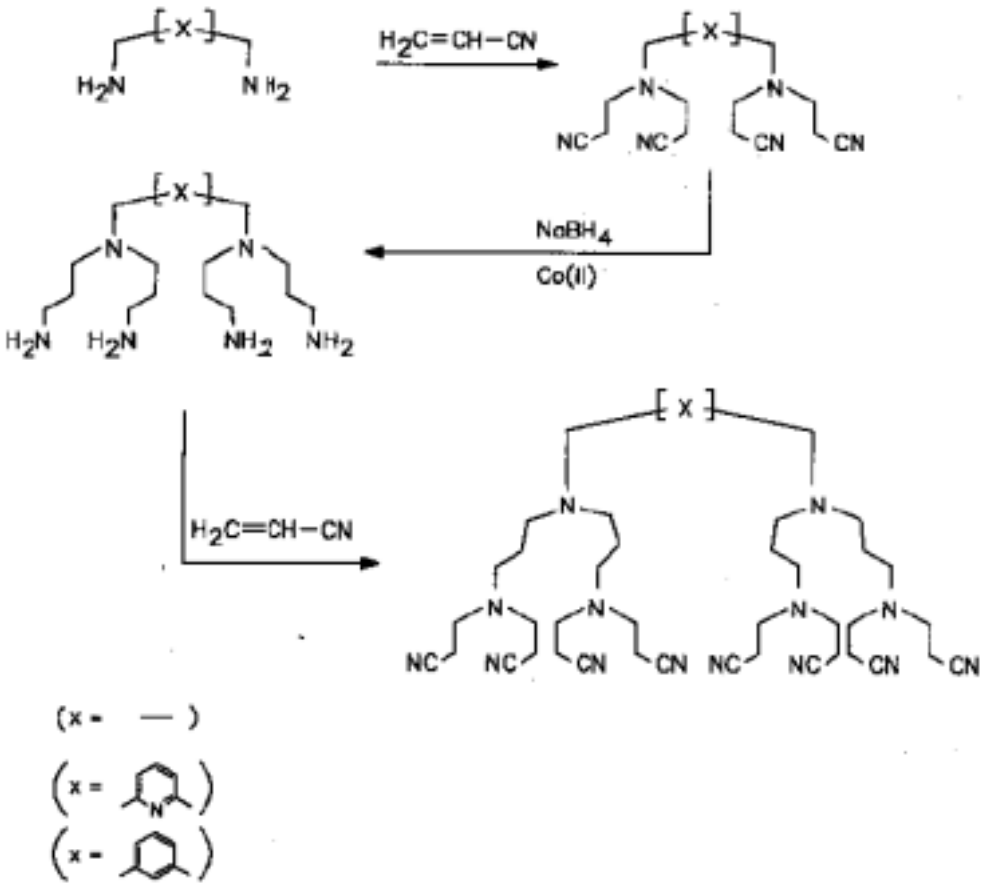

Figure 11.17. Original step-by-step self-assembly of a polyamine dendrimer by alternating between steps that replace the hydrogens of amino groups by cyanide groups [$-NH_2 \Rightarrow -N(CN)_2$], and then add hydrogens to the cyanide nitrogens [$-CN \Rightarrow -CNH_2$]. [From E. Buhleier, W. Wehner, and F. Vögtle, *Synthesis* **155** (1978).]

5th Generation PAMAM

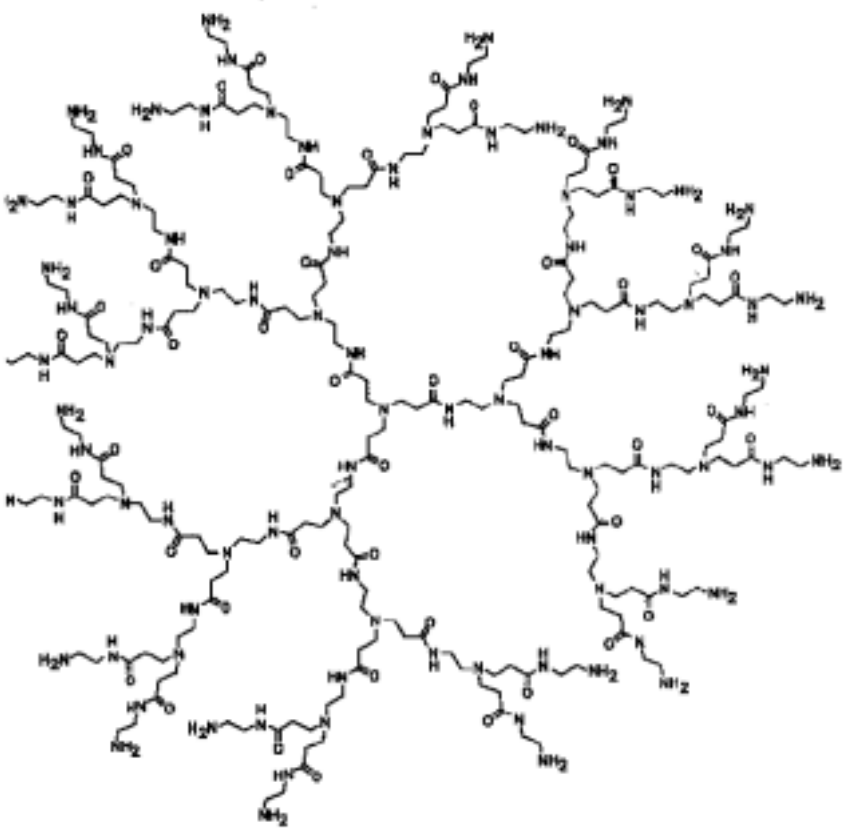

Figure 11.16. Fifth-generation polyamidoamine (PAMAM) dendrimer. [Prepared by D. A. Tomalia, H. Baker, J. R. Dewald, M. Hall, G. Kallos, S. Martin, J. Roeck, J. Ryder, and P. Smith, *Polym. J.* **17**, 117 (1985).]

dendralysts

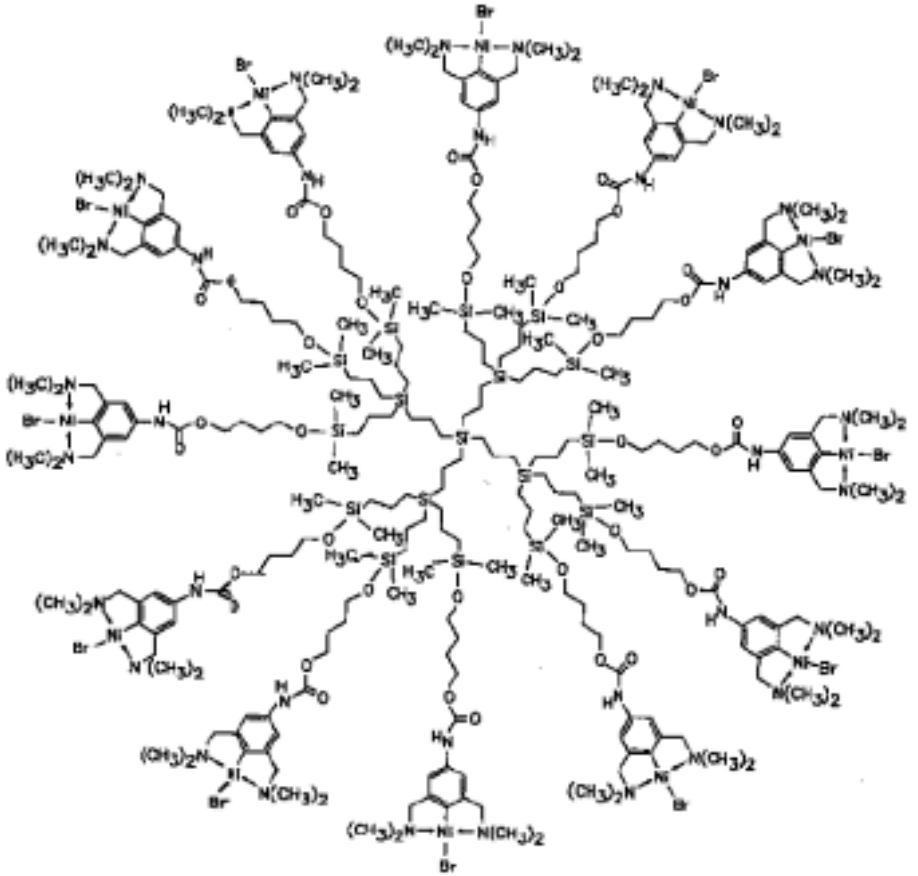

Figure 11.19. Dendrimer catalyst (dendralyst) with an Si core, and terminal group aryl–nickel complexes as the catalytically active functional groups. [From J. W. J. Knapen, A. W. van der Made, J. C. de Wilde, P. W. N. M. van Leeuwenn, P. Wijkens, D. M. Grove, and G. van Koten, *Nature* **372**, 659 (1994).]

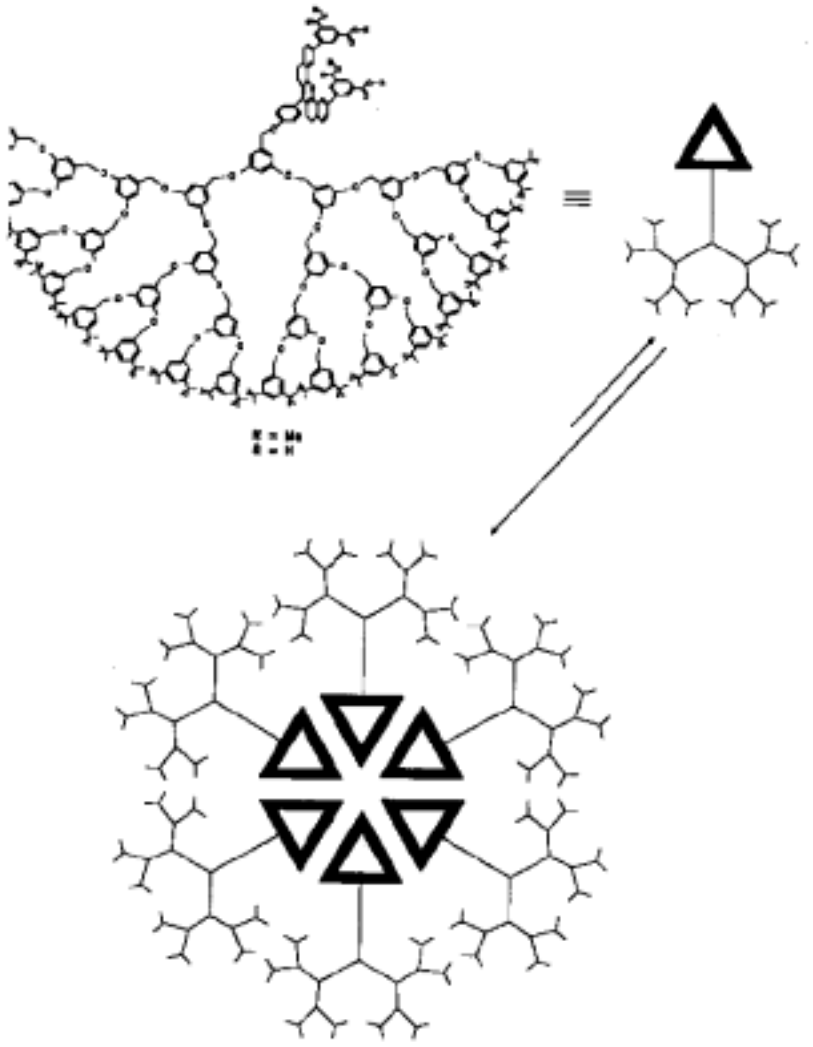

Figure 11.20. Sketch of sixfold (hexamer) supramolecular dendritic complex showing the structural formula of an individual component dendrimer at the upper left, the same component in a compact notation at the upper right, and the final self-assembled configuration of six components at the bottom. [Adapted from A. Archut and F. Vögtle, in Nalwa (2000), Vol. 5, Chapter 5, p. 367.]

Chapter 12

Biological Materials

12.2 Size of the biomaterials

DNA . $\phi = 2$ nm , unit $= 0.34$ nm

amino acid unit ~ 0.62 nm

$$d = 0.1184 \left(\frac{M_w}{\rho}\right)^{1/3}$$

$\rho = 1.45$

1.6 $\Rightarrow$ $d = 0.12 (M_w)^{1/3}$

1.3

1

68 kD $\rightarrow$ $d \sim 5$ nm

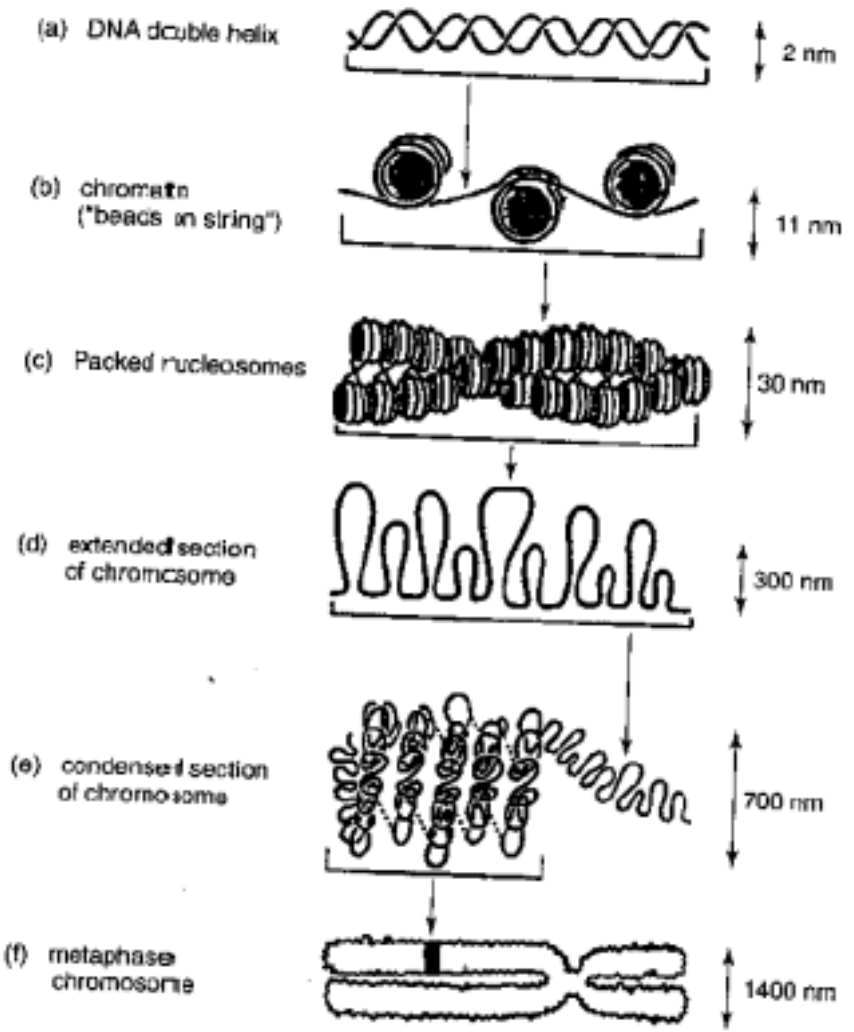

Figure 12.11. Successive twistings and foldings during the packing of DNA into mammalian chromosomes, with the sizes at successive stages given in nanometers. [From R. J. Nossal and H. Lecar, *Molecular and Cell Biophysics*, Addison-Wesley, Boston, 1991, Fig. 4.9 (p. 118).]

12.4.2 Micelles and Vesicles

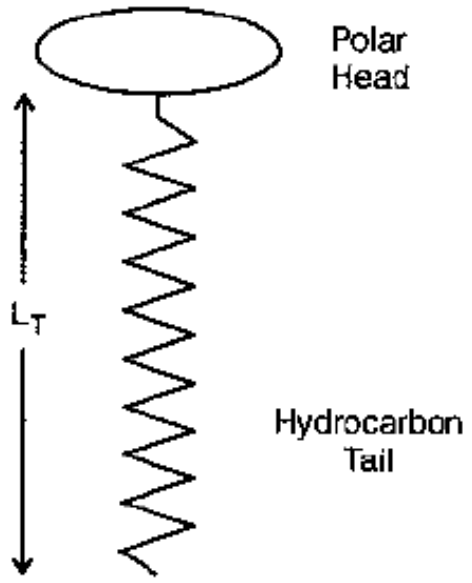

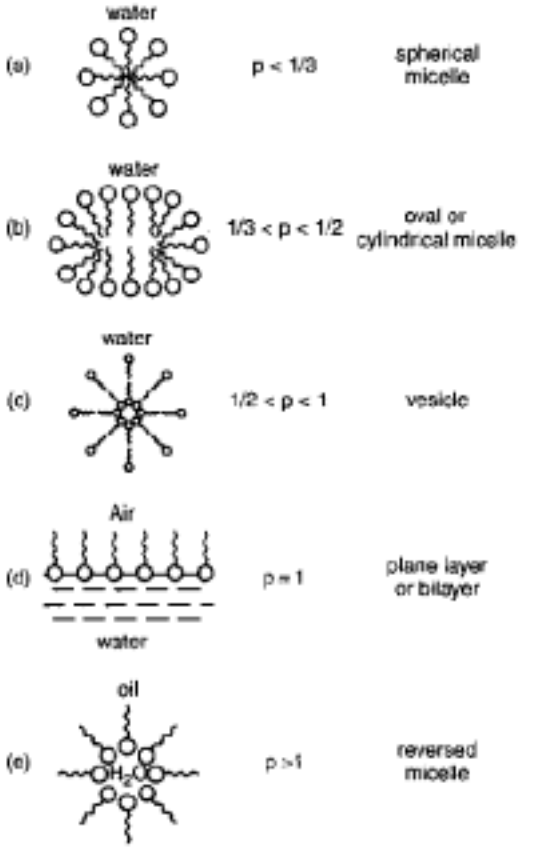

$$P = \frac{A_T}{A_H} = \frac{V_T}{A_H L_T}$$

Figure 12.14. Sketch of structures formed by amphiphilic molecules at water–oil or water–air interfaces for various values of the packing parameter p of Eq. (12.6). [Adapted from E. Nakache et al., in Nalwa (2000), Vol. 5, Chapter 11, p. 580.]

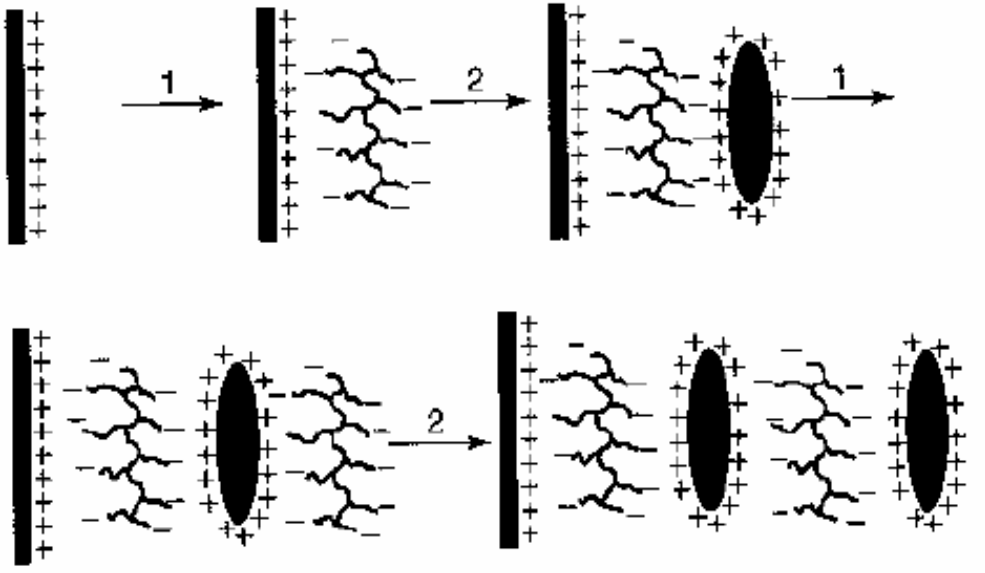

Figure 12.16. Sketch of the sequential adsorption process for the formation of a polyion film. The upper figure shows a positively charged substrate (left) that has adsorbed a negatively charged polyelectrolyte by being dipped into a negative electrolyte solution (center), and then adsorbed a positively charged layer from a positive electrolyte solution (right). The lower figure shows two additional steps in the sequential adsorption process. [From T. M. Cooper, in Nalwa (2000), Vol. 5, Chapter 13, p. 720.]